

Pluto's Ultraviolet Spectrum, Surface Reflectance, and Airglow Emissions

ANDREW J. STEFFL,¹ LESLIE A. YOUNG,¹ DARRELL F. STROBEL,²
JOSHUA A. KAMMER,³ J. SCOTT EVANS,⁴ MICHAEL H. STEVENS,⁵
REBECCA N. SCHINDHELM,⁶ JOEL WM. PARKER,¹ S. ALAN STERN,³
HAROLD A. WEAVER,⁷ CATHERINE B. OLKIN,¹ KIMBERLY ENNICO,⁸
JAY R. CUMMINGS,⁴ G. RANDALL GLADSTONE,³ THOMAS K. GREATHOUSE,³
DAVID P. HINSON,⁹ KURT D. RETHERFORD,³ MICHAEL E. SUMMERS,¹⁰ AND
MAARTEN VERSTEEG³

¹*Southwest Research Institute
1050 Walnut Street, Suite 300
Boulder, CO 80302, USA*

²*The Johns Hopkins University
Baltimore, MD*

³*Southwest Research Institute
San Antonio, TX*

⁴*Computational Physics Incorporated
Springfield, VA*

⁵*Naval Research Laboratory
Washington, DC*

⁶*Ball Aerospace
Boulder, CO*

⁷*Johns Hopkins University Applied Physics Laboratory
Columbia, MD*

⁸*SOFIA Science Center
Moffett Field, CA*

⁹*SETI Institute
Mountain View, CA*

¹⁰*George Mason University
Fairfax, VA*

(Received November 2, 2018; Revised March 20, 2020; Accepted April 24, 2020)

Accepted by AJ

ABSTRACT

During the New Horizons spacecraft's encounter with Pluto, the Alice ultraviolet spectrograph conducted a series of observations that detected emissions from both the interplanetary medium (IPM) and Pluto. In the direction of Pluto, the IPM was found to be 133.4 ± 0.6 R at Lyman α , 0.24 ± 0.02 R at Lyman β , and < 0.10 R

at He I 584Å. We analyzed 3,900 s of data obtained shortly before closest approach to Pluto and detect airglow emissions from H I, N I, N II, N₂, and CO above the disk of Pluto. We find Pluto’s brightness at Lyman- α to be $29.3 \pm 1.9R$, in good agreement with pre-encounter estimates. The detection of the N II multiplet at 1085Å marks the first direct detection of ions in Pluto’s atmosphere. We do not detect any emissions from noble gasses and place a 3σ upper limit of 0.14 R on the brightness of the Ar I 1048Å line. We compare pre-encounter model predictions and predictions from our own airglow model, based on atmospheric profiles derived from the solar occultation observed by New Horizons, to the observed brightness of Pluto’s airglow. Although completely opaque at Lyman α , Pluto’s atmosphere is optically thin at wavelengths longer than 1425Å. Consequently, a significant amount of solar FUV light reaches the surface, where it can participate in space weathering processes. From the brightness of sunlight reflected from Pluto, we find the surface has a reflectance factor (I/F) of 17% between 1400-1850Å. We also report the first detection of an C₃ hydrocarbon molecule, methylacetylene, in absorption, at a column density of $\sim 5 \times 10^{15} \text{ cm}^{-2}$, corresponding to a column-integrated mixing ratio of 1.6×10^{-6} .

Keywords: planets and satellites: atmospheres — Kuiper belt objects: individual (Pluto) — ultraviolet: planetary systems

1. INTRODUCTION

Pluto’s atmosphere was definitively discovered in 1988 by the technique of stellar occultation (Elliot et al. 1989; Hubbard et al. 1988), but its composition was unknown. The composition was subsequently deduced to be primarily N₂ with trace amounts of CH₄ and CO, based on detection of their ices on Pluto’s surface and their vapor pressures (Owen et al. 1993). Gaseous CH₄ was later detected spectroscopically (Young et al. 1997; Lellouch et al. 2017). As of the launch of NASA’s New Horizons spacecraft in 2005, only upper limits had been placed on the amount of atmospheric CO (Young et al. 2001; Bockelée-Morvan et al. 2001). The first detections of gaseous CO were claimed in 2011 (Lellouch et al. 2011; Greaves et al. 2011), and high SNR measurements of gaseous CO and HCN were made near-in-time to the New Horizons flyby with ALMA (Lellouch et al. 2017).

Shortly after the New Horizons spacecraft’s closest approach to Pluto, the Alice instrument observed an occultation of the sun by Pluto (Gladstone et al. 2016), while the Radio Science Experiment (REX) observed an occultation of Earth (Hinson et al. 2017). From the solar occultation, Alice detected absorption by N₂, CH₄, C₂H₂, C₂H₄, C₂H₆, and haze (Young et al. 2018). From the egress of the Earth occultation, which occurred over the Sputnik Planitia region, REX found that Pluto’s atmosphere was much colder (39 K at the surface, 65-68 K in the upper atmosphere) and more compact than expected prior to the flyby.

We report here observations of Pluto's atmosphere and surface by the Alice far ultraviolet (FUV) spectrograph onboard New Horizons, (Stern 2008) just prior to its closest approach.

2. THE ALICE FUV SPECTROGRAPH

Alice is a lightweight (4.4kg), low-power (4.4W), imaging, far ultraviolet (FUV) spectrograph (Stern et al. 2008). Sometimes referred to as "P-Alice" (for "PERSI-Alice", a precursor instrument design, or "Pluto-Alice"), to distinguish it from its older sibling instrument on ESA's Rosetta Spacecraft (Stern et al. 2007) consists an off-axis telescope feeding a 15-cm diameter Rowland-circle spectrograph with a wavelength range of 520-1870Å and a Nyquist-sampled spectral resolution of 3.8Å. The detector is an imaging microchannel plate (MCP) shaped to match the instrument's Rowland circle, coupled with a double delay line readout anode that converts the location of the charge cloud produced by the MCP into a 1024x32 (spectral x spatial) element data array, the central 740x21 pixel region in the data space maps to the illuminated area of the microchannel plate, with each of the 21 rows subtending a 0.3-degree angle on the sky (Siegmund et al. 2000). The front surface of the MCP is coated with a KBr photocathode layer that covers the passband of roughly 520-1160Å, a photocathode-free region covering 1160-1280Å and a CsI photocathode region covering 1280-1870Å. This photocathode regime was chosen to optimize efficiency at the extremes of the passband while minimizing the sensitivity to photons from the relatively bright Lyman α emission line, which, if not attenuated, would partially overwhelm the detector electronics.

The Alice instrument has two entrance apertures, the primary 40 mm x 40 mm square airglow aperture, co-aligned with the LORRI and Ralph instruments, and a secondary, 1 mm diameter circular solar occultation aperture (SOCC) offset by $\sim 90^\circ$ to the airglow aperture and roughly co-aligned with the Radio Science Experiment (Tyler et al. 2008) field of view (FOV). The data analyzed here were all obtained using the airglow aperture.

As seen from the detector, the Alice entrance slit is 6° long in the spatial dimension and divided into two sections: a narrow, rectangular region referred to as the "stem" and a wide, square region referred to as the "box". The stem is 4° in angular length along the spatial direction and 0.1° in the spectral dimension. The optical axis of the instrument is located 3° from the bottom of the stem, on the centerline of the 0.1° -wide slit. The stem portion of the slit corresponds to approximately rows 6–18 (zero-indexed) in data space, with the center of data row 16 defining the instrument boresight for spacecraft pointing purposes. The box is a $2^\circ \times 2^\circ$ angular width square, located at the top (higher detector row numbers) of the stem. The large width of the box was chosen so that even if there was a significant misalignment between the Alice solar occultation aperture and REX, both instruments would be able to simultaneously observe the occultations of the Sun and the Earth by Pluto's atmosphere.

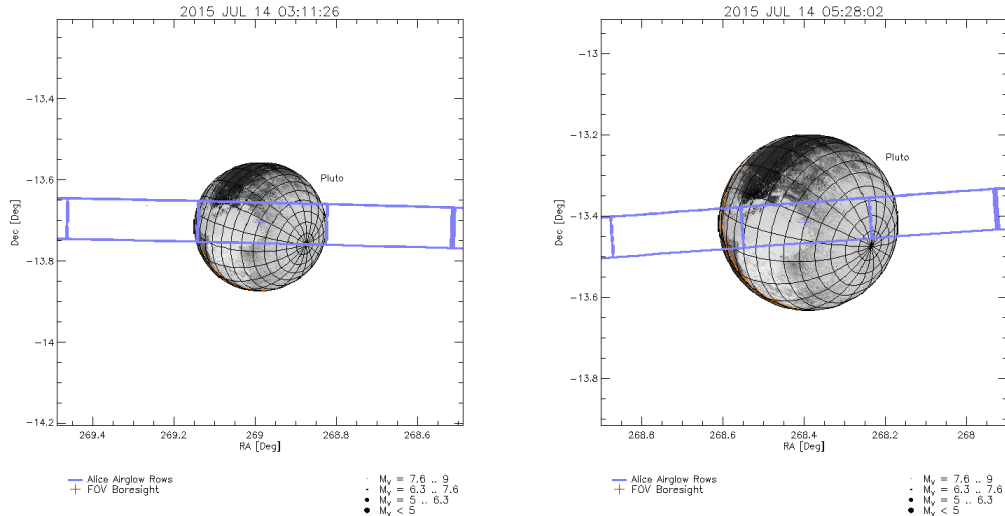


Figure 1. Observing geometry during the Airglow3 observation (left) and selected exposures from the Airglow4 observation (right). The projection of the Alice entrance slit onto the sky plane is outlined in blue. The approximately vertical, blue lines delineate the field of view of individual detector rows, with row 16 (zero indexed) lying on the disk of Pluto and rows 17 and 15 to the left and right of Pluto, respectively.

The box portion of the slit corresponds to rows 19-25, with row 18 serving as the transition between the two slit widths.

3. AIRGLOW OBSERVATIONS AND PROCESSING

On approach to Pluto, Alice made numerous observations in search of airglow emissions. For our analysis, we selected data from just two separate airglow observations, PEAL_01_PC_Airglow_Appr_3 and PEAL_01_PC_Airglow_Appr_4, hereafter Airglow3 and Airglow4. These particular observations were chosen because they are the closest, long-duration airglow observations of Pluto and thus, presumably, the most sensitive. Additionally, these observations have a favorable viewing geometry in which Alice is centered on Pluto, whose disk fills $>98\%$ of the field of view of the central row of the detector (row 16, zero-indexed). This minimizes the possibility of confusing emission from the interplanetary medium (IPM) with Plutogenic airglow emissions. The adjacent detector rows, 15 and 17, are centered at a tangent altitude of ~ 890 km and cover a region from the surface to a tangent altitude of 1.6 Pluto radii. Figure 1, produced using the web-based GeoViz tool (Throop et al. 2009), illustrates the observing geometry during the Airglow 3 & 4 observations. The instrument footprint covers a significant fraction of Sputnik Planitia as well as regions poleward.

Data from the Airglow3 observation consist of ten 300-second histogram exposures obtained from 2015 July 14 03:11:26 to 2015 July 14 04:01:26 UTC. During these exposures, the distance to Pluto spanned 427,621–386,306 km and the phase angle increased slightly from 16.90° to 17.09° . We also selected six, 150-second histogram exposures from the 18 exposures of the Airglow4 observation that covered a similar region on Pluto as Airglow3. These Airglow4 images were obtained from 2015 July 14

Table 1. Details of Airglow Observations

Observational Quantity	Airglow3	Airglow4
Number of integrations	10	6
Total integration time (s)	3,000	900
Start Time	2015 July 14 03:11:26	2015 July 14 05:20:31
End Time	2015 July 14 04:01:26	2015 July 14 05:35:31
Distance to Pluto at start (km)	427,600	386,300
Distance to Pluto at end (km)	321,000	308,600
Pluto phase angle at start ($^{\circ}$)	16.90	17.09
Pluto phase angle at end ($^{\circ}$)	17.51	17.60

05:20:31 to 2015 July 14 05:35:31 UTC and spanned 320,976–308,588 km in distance and 17.51–17.60 $^{\circ}$ in phase angle. To maximize the signal-to-noise ratio in the data, we co-added all 16 spectra. Observational details are shown in Table 1.

We apply the standard Alice data reduction techniques of dead time correction, stim pixel correction, and dark subtraction. These are described in more detail in the Appendix, below. As discussed above, there is no photocathode coating on the microchannel plate in the region around Lyman α (1216Å). This causes the extended wings of the line profile to appear to drop to zero, increase sharply around 60 Å from Lyman α (where the CsI and KBr photocathode coatings begin) and then decrease gradually with further distance from the line center. Because Lyman α emission line is so intrinsically bright, the extended wings of the line profile are comparable in intensity to the faint airglow emissions we are searching for—even several hundred angstroms away from core of the line. Thus, careful removal of the scattered Lyman α profile is required.

We created a Lyman α template image by summing 38 hours of Alice observations (PC_AIRGLOW_DOY, where DOY is the day of year), made on approach to Pluto between 2015 May 29 (DOY 149) and 2015 June 18 (DOY 169). Owing to the large distance of New Horizons to Pluto (greater than 30 million kilometers), no airglow emissions or sunlight reflected from Pluto were detected in these data, and Pluto’s disk blocks out an insignificant fraction of the field of view. In half of these observations, Pluto was placed at the center of the box portion of the slit and in the other half, Pluto was placed at the instrument boresight in the stem. No significant differences were seen between the two pointings. IPM emission lines were detected at Lyman α (1216Å) and Lyman β (1026Å) but not at HeI 584Å. The observed brightness (or upper limit) of these lines is given in Table 2. The brightness of the IPM Lyman α is $\sim 1.5\times$ brighter than pre-encounter predictions (Gladstone et al. 2015).

Since interplanetary Lyman β emission is $\sim 500\times$ fainter than Lyman α emission, the extended wings of its line profile are not significant. To prevent the unintentional subtraction of the IPM Lyman β signal from the Pluto observations, we fit a Gaus-

sian line profile with a linear background, to the IPM spectrum around 1026Å and subtract off the Gaussian component. The resulting template image contains only interplanetary Lyman α and detector dark counts. We remove these dark counts by subtracting a composite “dark” image, obtained while the airglow aperture door was closed. The spectrum of these dark counts can be seen in the blue line of Figure 2. After subtracting the scaled dark image from the Pluto observations, we normalize the IPM Lyman α template to the brightness of the Lyman α emission in the Pluto data.

Due to the slight misalignment of the Alice detector and the optical axes of the spectrograph, emissions that are centered in a given detector row at short wavelengths will partially spill over onto the next lower detector row for wavelengths greater than $\sim 1570\text{\AA}$. We therefore extract the airglow spectrum from row 16 and add the spectrum of row 15 to it for $\lambda > 1570\text{\AA}$. The resulting uncalibrated spectrum of Pluto is shown in Figure 2. We divide by the instrument’s effective area curve and by the solid angle of the sky as seen by a single detector row (0.3° spatial along the slit by 0.1° across it) to calibrate the spectrum in units of radiance.

4. PLUTO’S ATMOSPHERIC TRANSMISSION AND SURFACE REFLECTANCE

The observed spectral radiance of Pluto over the Alice passband is shown in Figure 3. The central spectral feature is the Lyman α airglow at 1216Å. Since the disk of Pluto completely fills the FOV of the central row during this observation, there is no contribution from the IPM. Faint airglow emission features arising from molecular, atomic and ionized species (e.g., N₂ CY(0,1) 980Å, N I 1493Å, and N II 1085Å) are present in the spectrum and are discussed in Section 5, below.

At wavelengths greater than $\sim 1500\text{\AA}$, Pluto’s spectrum is dominated by sunlight passing through the atmosphere and reflecting off the surface. Scattering of sunlight by atmospheric haze particles 100-200 km above the surface may also contribute a small amount to the observed spectrum at these wavelengths. For our purposes, the reflected/scattered solar light serves as an additional source of background that potentially obscures fainter airglow emissions in this region of the spectrum. We therefore

Table 2. Brightness of IPM lines from New Horizons (r=32.6 AU) in the direction of Pluto^a

Species	Wavelength (Å)	Observed Intensity ^b (R)
He I	584	< 0.10
H I	1026	0.24 ± 0.02
H I	1216	133.4 ± 0.6

^a $\alpha=18^h2^m38.7^s$, $\delta = -14^\circ37'37''.2$

^bQuoted error bars are 1σ , while the He I 584Å upper limit is 3σ

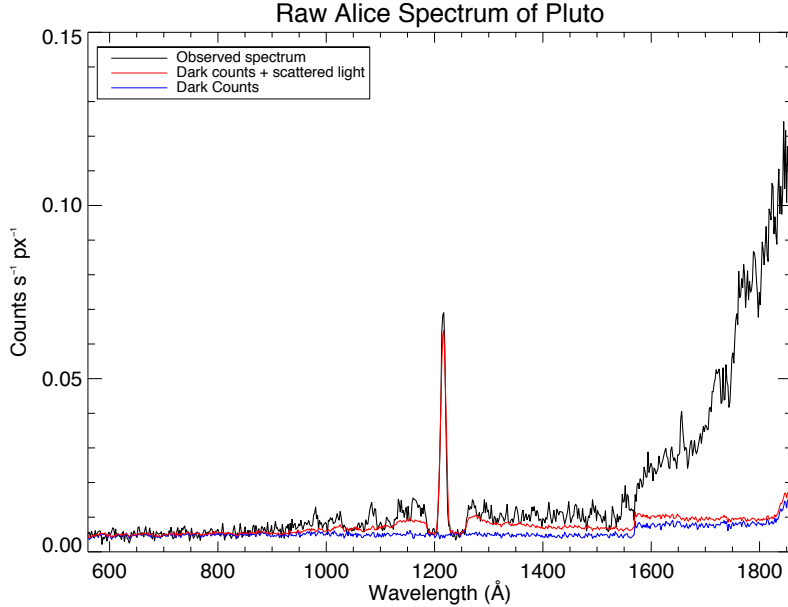


Figure 2. Alice count rate spectra of Pluto and background sources. The spectra are extracted from detector row 16, except for wavelengths longer than 1570\AA , which also include row 15. This causes the apparent jump in background rates. The black curve shows the uncalibrated count rate spectrum from the sum of the Airglow3 and Airglow4 observations used in this analysis. The blue curve shows the dark count background produced by the detector when the airglow aperture door is closed, and the red curve shows the sum of the dark count spectrum and the IPM Lyman α profile, scaled to the level of Lyman α in the Airglow3 observations.

attempt to remove the solar contribution by constructing a simple model of Pluto's atmospheric transmission and surface reflectance, based on the solar occultation profiles of Pluto's atmosphere (Young et al. 2018).

4.1. Atmospheric Transmission

The ingress and egress solar occultation profiles reported by Young et al. (2018) are largely similar. To increase the signal-to-noise in our analysis, we averaged the two occultation profiles together and re-binned the data to 25 km vertical resolution. We used this profile to reproduce the results of Young et al. (2018). Pluto's hazes are complex (Cheng et al. 2017; Zhang et al. 2017; Krasnopolsky 2020), and we do not attempt to derive a column density directly from the occultation profiles. Rather, following Young et al. (2018), we treat the haze as a spectrally-neutral source of atmospheric opacity in our fits to the solar occultation transmission spectrum. For comparison with other atmospheric constituents, we assume a wavelength-independent haze cross section of $1 \times 10^{-15} \text{ cm}^2$. With the additional assumption of spherical symmetry (reasonable, given the similarity of the ingress and egress profiles) we can apply the

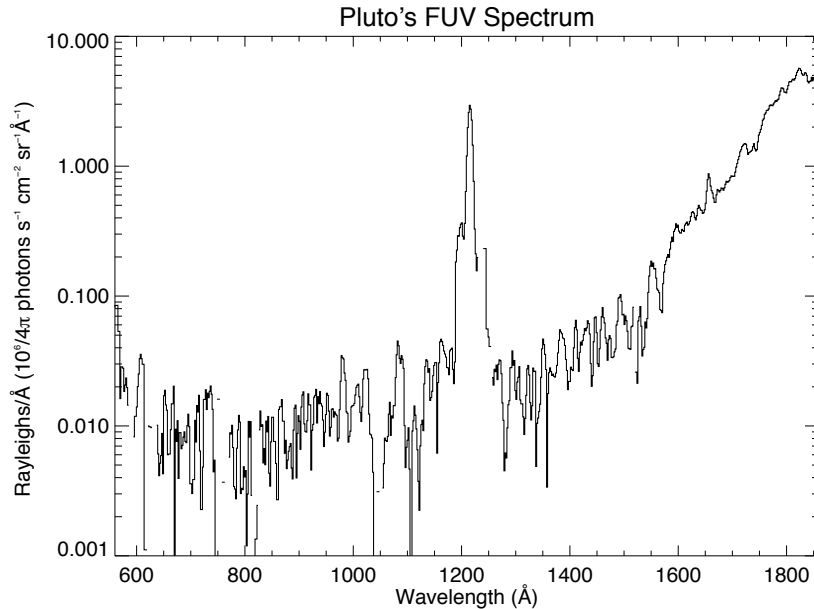


Figure 3. Observed spectral radiance of Pluto over the Alice passband. Both dark counts and a scattered Lyman α profile have been subtracted from the data. The dramatic increase in flux at the long wavelength end of the spectrum is the result of sunlight reflected from the surface of Pluto with a small contribution from sunlight scattered by atmospheric haze particles.

Abel transform (Roble & Hays 1972) to derive local number density from line-of-sight abundances (column densities):

$$n(r) = -\frac{1}{\pi} \int_r^\infty \frac{[dN(r')/dr']}{\sqrt{r'^2 - r^2}} dr', \quad (1)$$

where $n(r)$ is the number density of a given species at radial distance, r , from Pluto and $N(r')$ is the column density of that species at a tangent radius, r' . The resulting atmospheric profiles are shown in Figure 4, which is broadly similar to Figure 17 of Young et al. (2018).

As shown in Figure 1, the Alice field of view covered a significant fraction of the disk of Pluto during the Airglow 3 and 4 observations, and as such covers a large range of solar incidence and emission angles. Therefore, we divided the field of view of the central detector row (row 16, zero-indexed) into a grid of 31x11 lines-of-sight, separated by 0.01° (corresponding to a separation of roughly 70 km on Pluto's surface), and calculated the atmospheric absorption and surface reflection along each line of sight. Averaged over the Alice field-of-view, the solar incidence angle is 36.2° , while the average emission angle is 33.3° . We integrate the atmospheric profiles shown in Fig. 4 along the path from the sun to the surface and then from the surface to Alice for each of the 341 lines-of-sight. The two-way atmospheric transmission, averaged

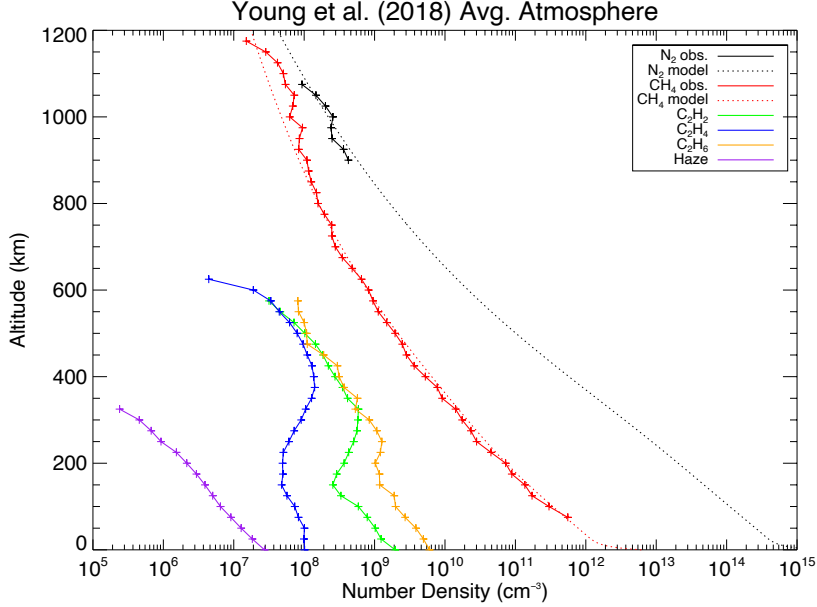


Figure 4. Atmospheric profiles of Pluto based on the solar occultation observations of Young et al. (2018). Dotted lines represent model fits to the observed N_2 and CH_4 profiles. Haze density is derived by assuming a wavelength-independent cross section of $1 \times 10^{-15} \text{ cm}^2$.

over the Alice field of view, is shown in the top panel of Figure 5, while the one-way vertical atmospheric transmission is shown in the bottom panel (cf. Figure 12 of Young et al. (2018)).

Pluto’s atmosphere is completely opaque at wavelengths below 1400 \AA , largely due to absorption by methane (CH_4). However, the absorption cross-section of methane decreases by more than four orders of magnitude between 1400 \AA and 1500 \AA , which results in the vertical optical depth of the atmosphere, τ_v , being less than one for $\lambda > 1425 \text{ \AA}$. Acetylene (C_2H_2) is the primary atmospheric absorber between 1430 - 1530 \AA , while at wavelengths greater than 1530 \AA , the atmospheric transmission is controlled by both haze particles and ethylene (C_2H_4).

As shown in the bottom panel of Figure 5 photons with $\lambda > 1425 \text{ \AA}$ readily pass through the atmosphere and interact with Pluto’s surface (i.e. $\tau_v < 1$). These photons have only $\sim 25\%$ less energy than Lyman α photons—enough to break molecular bonds and drive photolysis. (Olkin et al. 2017) report that Pluto’s equatorial regions, which receive greater insolation when averaged over Pluto’s orbit, are darker and redder than the poles, which are brighter and more neutral in color. They propose that this surface color distribution could be produced by the transport of volatiles away from the warmer equator towards the colder poles. We suggest that in addition to this

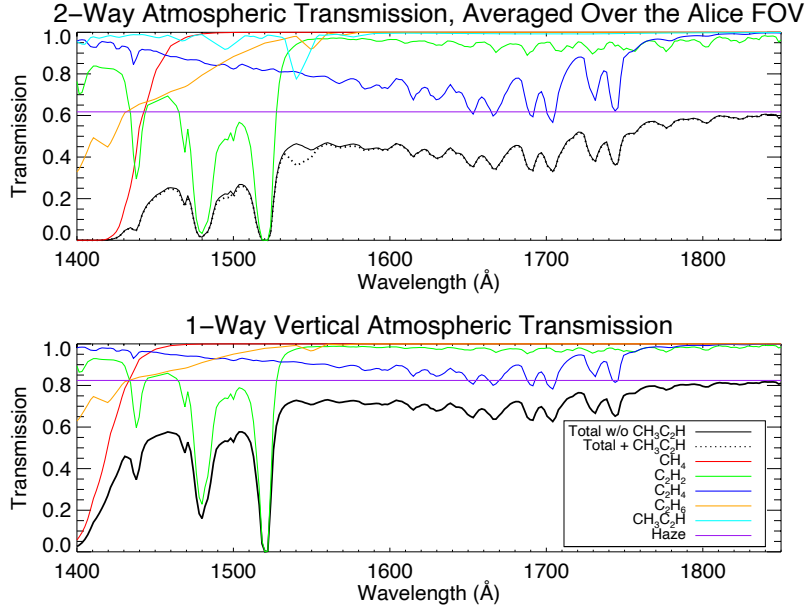


Figure 5. Top: 2-way transmission through Plutos atmosphere, averaged over the Alice field of view. We include atmospheric absorption from methane (CH_4), acetylene (C_2H_2), ethylene (C_2H_4), ethane (C_2H_6), and haze particles. The top panel also shows the additional absorption by $\sim 5 \times 10^{15} \text{ cm}^{-2}$ of methylacetylene (C_3H_4 along the line-of-sight (see discussion in Section 4.3). The detailed properties of the haze are not modeled. Instead, the haze is assumed to have a wavelength-independent cross section of $1 \times 10^{-15} \text{ cm}^2$ for rough comparisons to other atmospheric constituents. Bottom: 1-way vertical atmospheric transmission.

mechanism, longer-wavelength FUV photons photolyze tholins and haze particles on the surface, further reddening the equatorial regions.

4.2. Pluto's FUV Surface Reflectance

The reflectance factor, sometimes referred to as I/F, is defined as:

$$I/F(\lambda) = \frac{\pi hc I(\lambda, \phi) r^2}{\mu_0 \Omega F_{\odot}(\lambda)} \quad (2)$$

where h is Planck's constant; c is the speed of light; I is the observed spectral intensity in photons $\text{s}^{-1} \text{ cm}^{-2} \text{ \AA}^{-1}$ as a function of wavelength, λ , at a given solar phase angle, ϕ ; r is the heliocentric distance of Pluto in AU; μ_0 is the cosine of the solar incidence angle, averaged over the field of view; $\Omega = 9.1 \times 10^{-6} \text{ Sr}$ is the solid angle subtended by a single row of the Alice detector; and F_{\odot} is the solar flux at 1 AU. After proper calibration, $I(\lambda, \phi)$ is what is actually measured by Alice. We use the same $F_{\odot}(\lambda)$ as in Young et al. (2018), which was assembled from SUMER reference spectra (Curdt et al. 2001) and observations from TIMED/SEE (Woods et al. 2005).

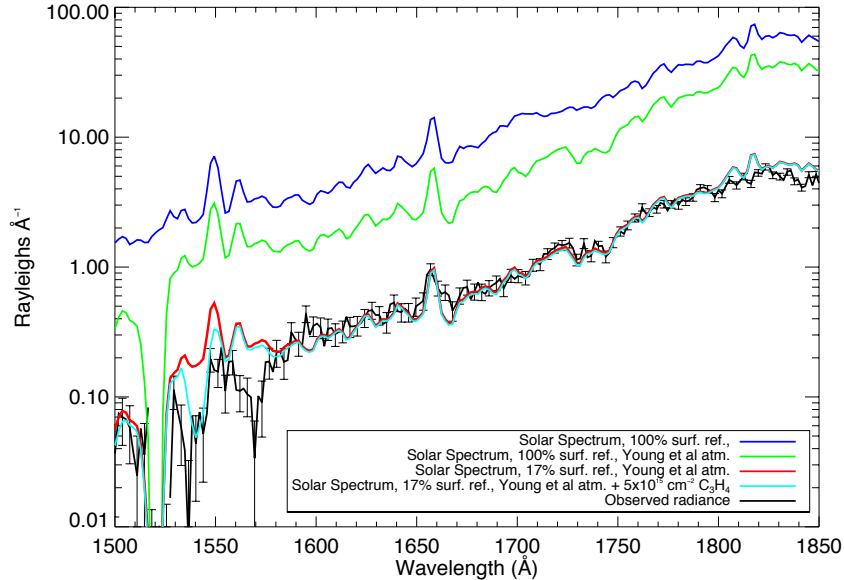


Figure 6. The observed spectral radiance of Pluto and solar spectra with various combinations of surface reflectance and atmospheric absorption. The spectral radiance observed by Alice is shown in black, with 1σ error bars shown for every other point. If Pluto had no atmosphere and a surface reflectance of 100%, Alice would observe the blue curve. Including absorption by the [Young et al. \(2018\)](#) atmosphere yields the green curve, while also reducing the surface reflectance to 17% produces the red curve—a surprisingly good match to the data for wavelengths longer than 1580Å. Between 1530–1580Å, there is an additional source/sources of absorption of the solar spectrum not included in [Young et al. \(2018\)](#) that results in an over-subtraction of the solar spectrum. Including absorption by methylacetylene (C_3H_4 or propyne) with a 2-way column density of $\sim 5 \times 10^{15} \text{ cm}^{-2}$ significantly improves the model fit between 1535–1550Å.

In the absence of an atmosphere and with a surface reflectance factor of 100%, the spectral radiance of Pluto would be about an order of magnitude greater than what is observed, as shown with the blue curve of Figure 6. Including the 2-way atmospheric transmission shown in Fig. 5 reduces our model spectral radiance to about $6 \times$ what is observed at long wavelengths. Combining this with a wavelength-independent surface reflectance factor of 17% yields a surprisingly good match to the observed radiance of Pluto at wavelengths greater than $\sim 1570\text{Å}$. Notably, the feature at 1657Å appears to be entirely due to the reflected/scattered solar C I multiplet and not airglow emission from Pluto’s atmosphere.

Compared to other planetary surfaces, an FUV I/F of 17% is relatively high. For example, comet 67P/Churyumov-Gerasimenko has an I/F of just 1–2% ([Stern et al. 2015](#)); Saturn’s moon, Phoebe, has a reflectance between 1–3% ([Hendrix & Hansen 2008](#)); while the Moon’s I/F varies between 2–10% ([Gladstone et al. 2012](#)).

As discussed above, Pluto’s atmospheric haze was treated simply as a source of extinction. In reality, haze particles will both scatter and absorb sunlight. Therefore, the 17% surface I/F value should really be thought of as an upper limit. Modeling the properties of Pluto’s atmospheric haze is well beyond the scope of this paper. However, as an end-member case, if we assume the haze particles are simple $0.2\mu\text{m}$ spheres with a single scattering albedo of 0.55 at 1500\AA , Mie scattering theory predicts that the haze will be roughly half absorbing and half scattering and that the scattering should be roughly independent with wavelength over the Alice pass band. If we then assume that as much sunlight is scattered back into our line-of-sight as out of it, a surface I/F value of 13% is required to match the Alice observations. We suggest that a more detailed analysis of Pluto’s ultraviolet surface reflectance, properly accounting for atmospheric haze, is a fruitful area for subsequent work.

4.3. Methylacetylene

While the overall match between the Alice observations and our simple transmission/reflectance model is fairly good, as shown in Fig. 6, our simple model predicts significantly more flux than is observed between $1535\text{--}1570\text{\AA}$, resulting in an over-subtraction of the solar spectrum. This suggests that either the atmosphere or surface has one or more additional sources of opacity/absorption. However, FUV absorption features from solids tend to be very broad, on the order of 100’s of Ångstroms (Wagner et al. 1987). Likewise, we are not aware of any mechanism by which atmospheric haze can produce such relatively narrow absorption features. Thus, we favor the interpretation that one or more additional gaseous species are present in Pluto’s atmosphere at high-enough column densities to significantly absorb sunlight passing through the atmosphere.

We examined the absorption cross sections of 32 additional atomic and molecular species that might plausibly be found in Pluto’s atmosphere (C, CH₃, CH₄O, C₂H, C₂H₅, C₃H₃, C₃H₄ (both the allene and methylacetylene isomers), C₃H₆ (both the propene and cyclopropane isomers), C₃H₈, C₄H₂, C₄H₄, C₆H₆, CO, CO₂, H, H₂, H₂CO, H₂O, H₂O₂, HCN, HC₃N, HNCO, N, NH₃, O, O₂, O₃, OCS, PH₃, SO, and SO₂), and found that, among them, only methylacetylene (H₃C–C≡CH, or propyne), has both a strong absorption band in this region and a lack of strong absorption bands at longer wavelengths, where no additional absorption is seen. Methylacetylene has been observed in the upper atmospheres of both Titan, where it can reach local mixing ratios of up to 10^{-5} (Li et al. 2015), and Jupiter, where it is part of an important chemical pathway in the production of acetylene (C₂H₂) (Gladstone et al. 1996). The Pluto photochemical model of Wong et al. (2017) predicts a methylacetylene column density of $2.5 \times 10^{15} \text{ cm}^2$ along our two-path line-of-sight. Including methylacetylene in our model at twice this value ($5 \times 10^{15} \text{ cm}^{-2}$; corresponding to a column-integrated mixing ratio of 1.6×10^{-6}) produces a significantly better fit around 1540\AA , as shown in Figure 6.

If absorption of reflected sunlight by methylacetylene is detectable in the airglow observations, it should also be evident in the solar occultation observed by Alice. Careful re-examination of the solar occultation profiles described by [Young et al. \(2018\)](#) over a range of tangent altitudes from 100-150 km shows a previously-unnoticed absorption feature at 1540Å, consistent with methylacetylene. Our preliminary re-analysis yields a methylacetylene column density of $1.5 \times 10^{15} \text{ cm}^{-2}$ along this line of sight. Since the analysis of the solar occultation observations involves only the transmission of sunlight through Pluto's atmosphere and we directly measure the unocculted solar spectrum, we can exclude the possibilities that this feature is caused by something in Pluto's surface reflectance spectrum or the solar spectrum itself. We therefore claim the first detection of a C₃-hydrocarbon in Pluto's atmosphere and suggest that an additional, yet-unidentified, atmospheric species is responsible for the apparent absorption features at 1530Å and 1570Å. The level of methylacetylene should provide an important constraint for future photochemical models of Pluto's atmosphere.

5. PLUTO'S AIRGLOW EMISSIONS

Pluto's extreme ultraviolet (EUV) airglow spectrum is shown in [Figure 7](#) and its far ultraviolet (FUV) spectrum, after subtracting the reflected solar spectrum, is shown in [Figure 8](#). (We loosely define the EUV region as wavelengths shorter than Lyman- α at 1216Å and the FUV as longer than Lyman- α but shorter than 2000Å.) Although the signal-to-noise ratio of the spectrum is relatively low throughout much of the bandpass, (observed count rates are generally on the order of 1 count/pixel/100 seconds), faint emission features from H I, N II, N I, N₂, and CO are detected at brightnesses of a few tenths of a Rayleigh ($\frac{10^6}{4\pi} \text{ photons s}^{-1} \text{ cm}^{-2} \text{ sr}^{-1}$). We discuss individual species in further detail in the subsections below.

To aid the identification of these features, we compare the observed airglow spectrum to a model spectrum produced by a version of the Atmospheric Ultraviolet Radiance Integrated Code (AURIC) ([Strickland et al. 1999](#); [Stevens et al. 2011, 2015](#); [Evans et al. 2015](#)) adapted to Pluto. AURIC generates emission spectra from multiple species as a function of viewing direction. In particular, it calculates emissions from solar fluorescence, electron impact, photoionization, photodissociation, and recombination and then propagates these emissions through a radiative transfer model of the atmosphere of interest. We generate emission spectra over the 800-2000Å bandpass. Since the Alice slit covers a significant fraction of the disk of Pluto, as discussed in [Sec. 4.1](#), we average the model output over an evenly-spaced grid of 341 lines of sight, separated by 0.01° ($\sim 70 \text{ km}$ projected on the surface). We start with the atmosphere of [Young et al. \(2018\)](#), as shown in [Fig. 4](#) and add CO at a surface mixing ratio of 5.0×10^{-4} ([Lellouch et al. 2017](#)), assuming that, like the rest of the atmosphere, it is in gravitational diffusive equilibrium.

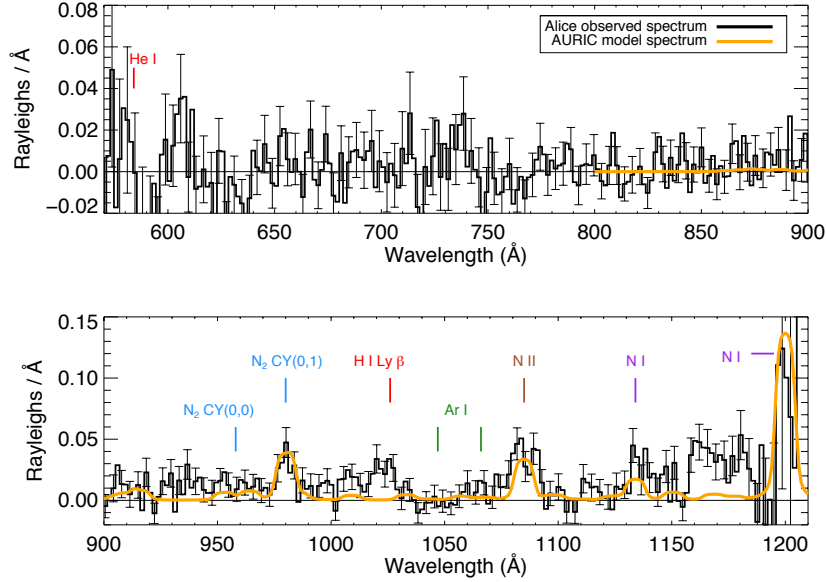


Figure 7. EUV airglow spectrum of Pluto. For clarity, every other error bar is plotted, representing the 1σ statistical uncertainty. At these wavelengths, Pluto’s atmosphere is opaque, and no reflected sunlight is present in the spectrum. Emissions from N_2 , $N II$, $N I$, and $H I$, are clearly detected. Notably absent are emission lines from argon at 1048\AA and 1067\AA . The orange curve is a synthetic spectrum produced by our AURIC model using the atmospheric profiles of Young et al. (2018) combined with surface mixing ratios of 5.0×10^{-4} for CO and 1.5×10^{-4} for $Ar I$. Our model does not include emissions from hydrogen. The elevated brightness between $1160\text{--}1190\text{\AA}$ is likely an artifact of the Lyman- α background subtraction.

AURIC produces synthetic spectra for molecular emission band systems and individual atomic species. For this paper, we did not vary the model’s input parameters in an attempt to fit the observed airglow spectrum in a fully self-consistent manner. Such work will be the subject of a future publication. However, recent analyses of the atmospheres of Mars and Titan using AURIC (Stevens et al. 2015; Jain et al. 2015; Schneider et al. 2015; Stevens et al. 2017), have shown that weighting each of the individual component spectra can result in a markedly better match to the data. We use a multiple linear regression (MLR) algorithm to determine the weights for each component spectrum:

$$S_{\text{final}}(\lambda) = \sum^n a_n S_n(\lambda) \quad (3)$$

where a_n are the weights for the individual component spectra, $S_n(\lambda)$, for each molecular band system or atom produced by our AURIC model. Our MLR fit has five component spectra: the Lyman-Birge-Hopfield (LBH) and Vegard-Kaplan (VK) band systems of N_2 , the Fourth Positive (4PG) and Hopfield-Birge (HB) band systems of

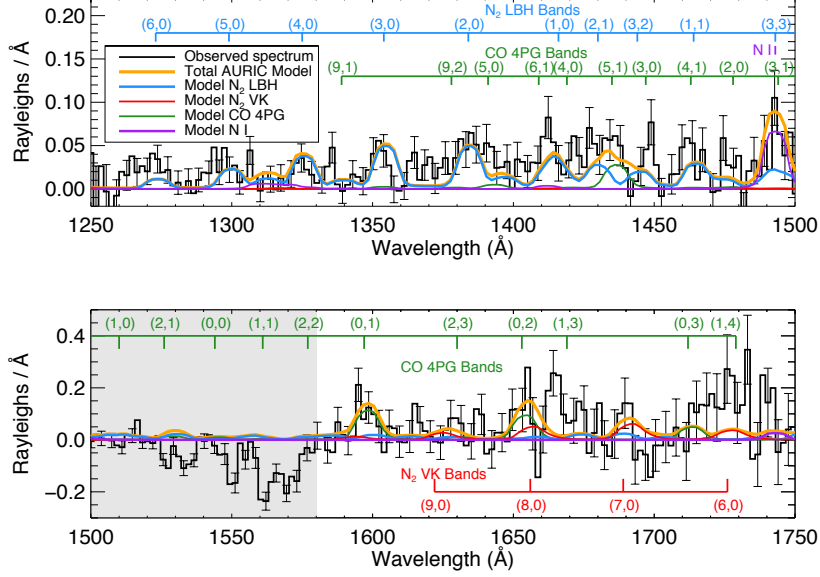


Figure 8. FUV airglow spectrum of Pluto with our AURIC model prediction. For clarity, every other error bar is plotted, representing the 1σ statistical uncertainty. Emissions from N_2 , NI and CO are detected. The orange curve is a synthetic spectrum produced by our AURIC model using the atmospheric profiles of [Young et al. \(2018\)](#) combined with surface mixing ratios of 5.0×10^{-4} for CO and 1.5×10^{-4} for Ar I. Between 1500–1580Å, there is a source of additional absorption in Pluto’s atmosphere or surface that is not included in our background model, resulting in an over-subtraction of the reflected solar spectrum (see Sec. 4). This region, shaded in gray, is excluded from further analysis.

Table 3. Integrated MLR model brightnesses ($800\text{Å} < \lambda < 2000\text{Å}$)

Emission	Intensity (R)	1σ error (R)
N_2 LBH bands	7.8	0.7
N_2 VK bands	3.3	1.6
CO 4PG bands	4.1	0.9
CO HB bands	0.17	0.08
N I	4.3	0.7

CO, and the emission multiplets of N I. The weights were simultaneously fit to the data over the following three bandpasses: $1100\text{Å} < \lambda < 1200\text{Å}$, $1270\text{Å} < \lambda < 1505\text{Å}$, and $1580\text{Å} < \lambda < 1750\text{Å}$. The model intensities of these emissions, integrated over $800\text{Å} < \lambda < 2000\text{Å}$ are given in Table 3.

Our model spectrum is a reasonably good match to the observations, as can be seen in Figures 7 and 8. All of the detectable emission features predicted by our model are either present in, or at least consistent with, the observed airglow spectrum. Conversely, there are no significant emission features predicted by our model that are clearly missing from the observed spectrum. On the other hand, there are several features in the observed spectrum that appear to be statistically significant but do not appear in our model. These are likely either instrumental artifacts or systematic effects of our data processing, and they are discussed in further detail in Section 5.7, below.

From the results of our AURIC model, we claim the detection ($> 4\sigma$ likelihood) of the N₂ LBH and CO 4PG bands. With a 2σ level of confidence, we also plausibly detect emissions from the N₂ VK bands, the brightest of which is predicted to be the (7,0) band at 1689Å. However, we advise caution in interpreting the CO HB bands as a ($\sim 2\sigma$) “detection”. This band system in the EUV is quite faint (< 0.2 R, integrated over the entire instrument bandpass), and while including it in the model does result in a statistically better fit, none of the predicted CO HB emissions (the brightest of which occur at 1151Å and 1124Å) are particularly compelling. We attempted to include the Birge-Hopfield-1 band system of N₂ and Cameron band system of CO in our MLR model, but found that these band systems were not sufficiently constrained by our data.

We detect airglow emissions from H I at both Lyman α and Lyman β and derive the amount of hydrogen above the $\tau = 1$ altitude in Section 5.1, below. Although this is an important constraint, we cannot measure the vertical profile of hydrogen in Pluto’s atmosphere from the Alice data or from any other currently existing observations. Since hydrogen is produced and destroyed by a large number of reactions in Pluto’s atmosphere and developing a full photochemical model is well beyond the scope of this observational paper, we do not include it in our AURIC model atmosphere. As neither H nor H₂ are a significant source of atmospheric opacity—at least for any physically reasonable amount of hydrogen—this omission does not affect the interpretation of other airglow spectral features.

In the EUV region of the spectrum, the airglow emission features are well-separated (see Fig 7). To determine their brightness (or upper limits), we fit a Gaussian line profile plus a linear background to each feature. The width of the Gaussian profile was held constant to match the line function of the instrument for a filled slit (Stern et al. 2008). The area under the fitted Gaussian profile (or the 3σ uncertainty thereof, in the case of a non-detection) is given in Table 4, along with model predictions from Summers et al. (1997), Stern et al. (2008), Young et al. (2008), Stevens et al. (2013), Jain & Bhardwaj (2015), and our MLR-weighted AURIC model.

The situation is more complicated in the FUV, as Pluto’s atmosphere transitions from completely opaque for wavelengths below 1400Å to $\tau < 1$ for $\lambda > 1540$ Å. Sunlight, reflected from the surface, overwhelms the faint airglow emissions at wavelengths

greater than $\sim 1400\text{\AA}$. Section 4 describes how we model the reflected sunlight and subtract it from the data. However, there appears to be an additional source of absorption in Pluto's atmosphere between $1500\text{\AA} < \lambda < 1580\text{\AA}$ that is missing from our model. This results in an over-subtraction of the solar spectrum, as can clearly be seen in Figure 8. We therefore exclude this region from all subsequent analysis.

In addition, at the spectral resolution of Alice, emissions from the N₂ LBH bands, the CO 4PG bands, NI, and the N₂ Vegard-Kaplan (VK) bands (in blue, green,

Table 4. Brightness of selected airglow emission features

Species	Wavelength (\AA)	Intensity ^a (R)	Model Predictions (R)					
			SSG97 ^b	SSS08 ^c	YSW08 ^d	SEG13 ^e	JB15 ^f	this work
HeI	584	< 0.49	–	–	–	–	–	–
NII	916	< 0.21	0.08	0.13	0.04	0.05	–	0.08
N ₂ CY(0,0)	958	< 0.20	0.7	1.3	0.35	0.0	–	0.0
N ₂ CY(0,1)	980	0.28 ± 0.08	–	–	–	0.2	–	0.4
HI	1026	0.20 ± 0.04	–	–	–	–	–	–
ArI	1048	< 0.14	0.3	0.45	0.15	0.3	–	2×10^{-4}
ArI	1067	< 0.21	0.3	0.35	0.15	0.3	–	2×10^{-4}
NII	1085	0.57 ± 0.14	0.4	0.6	0.2	0.2	–	0.30
NI	1134	0.25 ± 0.09	0.2	0.9	0.1	0.1	–	0.15
NI	1200	0.66 ± 0.64	1.2	5.4	0.6	0.7	–	1.3
HI	1216	29.3 ± 1.9	37	28	18	41	–	30 ^g
N ₂ LBH (4,0)	1325	0.14 ± 0.10^h	–	–	–	0.08	0.18	0.39
N ₂ LBH (3,0)	1354	0.20 ± 0.11^h	–	–	–	0.10	0.22	0.51
N ₂ LBH (2,0)	1383	0.40 ± 0.13^h	–	–	–	0.08	0.18	0.51
N ₂ LBH (1,1)	1464	0.59 ± 0.21^h	–	–	–	–	0.12	0.29
NI	1493	0.63 ± 0.18^h	–	–	–	0.23	–	0.68
CO 4PG (0,1)	1597	1.2 ± 0.4^h	–	–	–	0.0	2.0	1.2
CO 4PG (0,2)	1653	2.9 ± 0.9^h	–	–	–	0.0	–	1.0
N ₂ VK (7,0)	1689	1.0 ± 0.7^h	–	–	–	–	0.21	0.72

^aQuoted error bars are 1σ , while the upper limits are 3σ

^bSummers et al. (1997)

^cStern et al. (2008)

^dYoung et al. (2008)

^eStevens et al. (2013)

^fJain & Bhardwaj (2015)

^gIn the absence of H in our AURIC model, we report here the value predicted by Gladstone et al. (2015)

^hThis spectral feature is a blend of multiple emission lines/bands. We report the total intensity of the feature, as determined by a Gaussian fit.

purple, and red, respectively) are significantly blended together. Since we cannot separate these components observationally and do not have full confidence—at the level of individual spectral features—in the relative intensities predicted by our MLR model fit to the data, we report only the total brightness of each spectral feature.

5.1. *Hydrogen*

The bright emission line at Lyman α (1216Å) indicates that atomic hydrogen is present in Pluto’s upper atmosphere—a result of methane photochemistry. We find a Lyman α brightness of 29.3 ± 1.9 R, which matches the pre-encounter predictions by Gladstone et al. (2015) that relied on the model atmosphere of Krasnopolsky & Cruikshank (1999). The H I Lyman β emission line at 1026Å was also detected, though $\sim 150\times$ fainter than Lyman α . Since the Lyman α emission line is optically thick in Pluto’s atmosphere, we use the brightness, B (in units of Rayleighs), of the optically thin Lyman β line to estimate the hydrogen column density above the $\tau = 1$ level:

$$B = 10^{-6} g_{ik} N \quad (4)$$

where the “g-factor”, g_{ik} , is the number of radiative transitions per second per particle from quantum state k to state i . Chamberlain & Hunten (1987) define the g-factor as

$$g_{ik} = \frac{\pi e^2}{m_e c^2} \frac{A_{ki}}{\sum_j A_{kj}} \sum_j \frac{P_j \pi F_\odot \lambda_{jk}^2 f_{jk}}{r^2} \quad (5)$$

where the subscript j in the sums on the right is necessary to account for all possible paths to/from the upper level, k ; r is the heliocentric distance, in AU; F_\odot is the incident solar flux (in photons $\text{s}^{-1} \text{cm}^{-2} \text{Å}^{-1}$) at 1 AU (our F_\odot is identical to that described in detail by (Young et al. 2018)); A_{kj} is the Einstein “A” coefficient for the transition from state k to j ; f_{jk} is the oscillator strength for the upward transition from level j to level k ; and P_j accounts for the portioning of levels in the ground state, given temperature T :

$$P_j = \frac{(g_j + 1) e^{-\frac{E_j}{kT}}}{\sum_j (g_j + 1) e^{-\frac{E_j}{kT}}} \quad (6)$$

where g_j is the statistical weight of state j . We find a g-factor for Lyman β of $g_{1026\text{Å}} = 2.64 \times 10^{-9}$ photons s^{-1} . This implies a hydrogen column density of $N_H = 7.7 \pm 1.7 \times 10^{13} \text{cm}^{-2}$ and a LOS mixing ratio of $8.1 \pm 1.8 \times 10^{-5}$ above the $\tau = 1$ altitude of 490 km,.

5.2. *Argon*

Resonant scattering of the EUV solar continuum by argon produces emission lines at 1048Å and 1067Å, well within the bandpass of Alice. Little is known about the

relative abundance of argon in Pluto’s atmosphere or other objects in the Kuiper belt. Early observations of the atmosphere of Saturn’s moon, Titan, by Voyager IRIS placed an upper limit on the mixing ratio of argon at 6% (Courtin et al. 1995). This led Summers et al. (1997) to include argon at a constant mixing ratio of 5% in their Pluto atmospheric models, resulting in a predicted brightness of the Ar I 1048Å line of 0.3 R. More recently, Using the Krasnopolsky & Cruikshank (1999) “Model 2” atmospheric profile and an altitude-independent argon mixing ratio of 5%, Stern et al. (2008) predicted 0.45 R, and more recently, Mousis et al. (2013) predicted a brightness of 1.3 R—levels that should be detectable by New Horizons’ Alice. However, subsequent in situ measurements of Titan’s atmosphere by the Huygens probe gas chromatograph mass spectrometer reduced the Voyager-era upper limit on the mixing ratio of argon by more than three orders of magnitude to just $3.39 \pm 0.12 \times 10^{-5}$ (Niemann et al. 2010). The ultraviolet spectrograph on Cassini, UVIS, also failed to detect any emission from argon at Titan (Stevens et al. 2011), calling into question whether Alice would detect argon emission at Pluto.

Pre-flyby models of Pluto’s atmosphere that predicted detectable argon emission lines generally assumed a relatively warm, well-mixed atmosphere. Instead, New Horizons found an atmosphere that is considerably colder (a peak temperature of 106 K at 25 km altitude, falling to a nearly constant temperature of 68 K in the upper atmosphere) (Gladstone et al. 2016). At present, there are extreme discrepancies between various models of Pluto’s atmosphere. The model atmosphere of Young et al. (2018) has a very small eddy diffusion coefficient, resulting in an atmosphere with the well-mixed portion restricted to the planetary boundary layer (surface to 2 km). Above that, their atmosphere is in gravitational diffusive equilibrium. In contrast, the model atmosphere of Luspay-Kuti et al. (2017) has a much larger eddy diffusion coefficient, such that argon does not diffusively separate until an altitude of approximately 400 km.

We do not detect either argon emission line in the Alice data. We place a 3σ upper limit of 0.14 R on the brightness of the Ar I 1048Å line and 0.21 R on the Ar I 1067Å line. At these wavelengths, methane is the primary source of atmospheric opacity. For a CH₄ absorption cross section of 3.2×10^{-17} cm² at 1048Å (Kameta et al. 2002; Chen & Wu 2004), an optical depth of $\tau = 1$ is reached at a column density of $N_{CH_4} = 3.1 \times 10^{16}$ cm⁻². Averaged over the field of view, this occurs at an altitude of 480 km above Pluto’s surface (Young et al. 2018).

The g-factor for the Ar I 1048Å line at a heliocentric distance of 32.9 AU is 7.6×10^{-11} photons s⁻¹. Thus, to produce our 3σ upper limit of 0.14 R of Ar I 1048Å requires an Ar column density of 1.8×10^{15} cm⁻² above the $\tau = 1$ level. This is roughly 6% of the column of density of methane. For atmospheric models that use a small eddy diffusion coefficient (e.g. Strobel & Zhu (2017); Young et al. (2018)), the Alice detection limit isn’t significant, as even if the density of argon and (molecular) nitrogen were equal at Pluto’s surface, you would still expect brightness of the Ar I 1048Å line to be

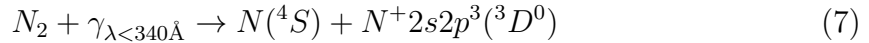
$\ll 0.14$ R. For atmospheric models with high eddy diffusion coefficients, such as [Luspay-Kuti et al. \(2017\)](#), the Alice results could be more physically meaningful.

5.3. NI

Several multiplets from atomic nitrogen are present in the airglow spectrum. The brightest of these occurs in the FUV at 1493Å, although this feature is blended with the CO fourth positive (3,1) band and the N₂ LBH (3,3) band. The EUV multiplets at 1200Å and 1134Å are also significant. The observed NI 1200Å multiplet is somewhat brighter than our AURIC model predicts. However, its proximity to the much brighter HI 1216Å emission line (and resulting scattered light results) in a low signal-to-noise ratio for this multiplet. Although this emission feature appears to be real, it is only present at the 1σ level of significance.

5.4. NII

One of the brighter features in Pluto’s EUV airglow spectrum is the NII 1085Å multiplet. This multiplet is produced primarily by the dissociative photoionization of molecular nitrogen by solar EUV and X-ray photons via excitation of the H band of N₂⁺ ([Samson et al. 1991](#); [Bishop & Feldman 2003](#)):



This NII 1085Å multiplet was also detected at both Triton ([Broadfoot et al. 1989](#)) and Titan ([Stevens et al. 2011](#)). The detection here marks the first, and thus far only, detection of ions in Pluto’s atmosphere (although the in situ instruments SWAP and PEPSSI measured ions escaping from Pluto’s atmosphere ([Bagenal et al. 2016](#))). Although this multiplet provides a direct detection of ion production in Pluto’s upper atmosphere, because it is a consequence of the dissociation of N₂ rather than the excitation of an existing ion, it cannot be used as a diagnostic of the ambient ion density.

5.5. N₂

The emission feature at 980Å is due to the N₂ Carroll-Yoshino (CY) $c_4' ^1\Sigma_u^+ - X^1\Sigma_g^+$ (0,1) band—an electronic transition. Although the CY (0,0) band is strongly excited by photoelectrons and its emission was predicted by [Young et al. \(2008\)](#) and [Stern et al. \(2008\)](#), it was not detected. This is because the CY (0,0) band is optically thick and strongly self-absorbed. After multiple scattering, much of the energy is ultimately radiated away via the optically thin CY (0,1) band ([Stevens et al. 1994](#); [Stevens 2001](#)). Both the Voyager UVS at Triton ([Broadfoot et al. 1989](#)) and the Cassini UVIS at Titan ([Ajello et al. 2007](#); [Stevens et al. 2011, 2013](#)) detected the CY (0,1) band but not the CY (0,0) band. We adapt a multiple scattering model for the CY (0,v”) bands used on Earth and Titan ([Stevens et al. 1994](#); [Stevens 2001](#)) to the Pluto atmospheric profiles derived from the occultation results shown in Figure 4. Excitation rates for

c_4' were calculated from AURIC and used to initialize the model. The redistribution of photons to more optically thin bands is calculated at milliångstrom resolution over multiple scatterings and at all altitude layers. We find that the CY(0,0) band is optically thick and undetectable at Pluto. In contrast, the nadir viewing CY(0,1) emission is found to be 0.4 R, which is close to what is observed and included in Table 4.

In addition to the CY (0,1) band, emissions at several of the LBH ($a^1\Pi_g-X^1\Sigma_g^+$) bands of N_2 are present in the spectrum at wavelengths greater than 1300Å (see Fig 8). Among these, the LBH (4,0), (3,0), and (2,0) bands at 1325Å, 1354Å, and 1383Å, respectively, are predicted to be the brightest. These features are present in the Pluto airglow spectrum, although at fairly low signal-to-noise levels. Many of the N_2 LBH bands overlap emissions from the CO fourth positive bands.

The N_2 Vegard-Kaplan (VK) bands ($A^3\Sigma_u^+-X^1\Sigma_g^+$) should also be present and marginally detectable in the airglow spectrum of Pluto at wavelengths greater than 1600Å. In the Alice bandpass, the brightest of these should be the (7,0) band at 1689Å. There appears to be a weak emission feature at this location. Other bands of the VK system are either too faint or too blended with other emissions to be clearly detected.

5.6. Carbon Monoxide

Just one month prior to the New Horizons flyby of Pluto, [Lellouch et al. \(2017\)](#) observed Pluto with the ALMA interferometer. They report the detection of CO in Pluto's atmosphere at a mole fraction of 515 ± 40 ppm, i.e, a surface mixing ratio of $\sim 5 \times 10^{-4}$. At this concentration, several of the bands of the CO fourth positive system ($A^1\Pi-X^1\Sigma^+$) should be detectable by Alice, although they will be blended with the N_2 LBH and VK bands. Almost all of the CO fourth positive bands are optically thick, requiring careful modeling of radiative transfer effects to extract column density from the observed brightness. Due to the saturation of the bands of the CO fourth positive group, Alice is not very sensitive to changes in CO column density. For example, our modeling with AURIC suggests that doubling the surface mixing ratio of CO leads to only a $\sim 10\%$ increase in the brightest CO fourth positive bands.

Given that, our model predicts the brightest CO emission features to be the (0,1), (0,2), (0,3), and (5,1) bands at 1597Å, 1653Å, 1712Å, and 1435Å, respectively, as shown in Fig 8. The first three of these bands are produced by the solar C IV 1548Å emission line exciting the nearby CO (0,0) band at 1544Å. Due to the large optical depth of the (0,0) band, much of this energy is radiated away via the (0,1), (0,2), and (0,3) bands. Similarly, the solar Si IV emission line at 1393.8Å pumps the CO (5,0) band at 1391.1Å and because of optical depth effects, this energy is primarily radiated away through the (5,1) band at 1435Å.

5.7. Other Features

None of the features below 920\AA are statistically significant. In particular, we do not detect any emission at He I 584\AA and place a 3σ upper limit of 0.49 R on the brightness of this emission line. Although there appears to be a 2σ significant emission feature at 736\AA , this is a known instrumental artifact (a Lyman- α ghost) and not emission from Ne I.

Between $1160\text{-}1180\text{\AA}$, our airglow spectrum is significantly elevated above the background level. This feature is too wide to be due to a single emission line or band, and none of the species that have been detected in Pluto’s atmosphere emit significantly in this bandpass. Nor are we aware of any ions/atoms/molecules that might plausibly contribute to these putative emissions while producing no other detectable UV signature. We therefore believe this feature is likely an artifact of our data processing.

Similarly, there are several features in the FUV that appear to be significant at about the 2σ level, yet do not correspond to the wavelength or predicted intensity of any known emissions. Examples include the feature at 1412\AA , which is both longward of the CO Fourth Positive (6,1) band and shortward of the N_2 LBH (1,0) band, and the feature at 1449\AA , which could plausibly be the CO Fourth Positive (3,0) band, except that our AURIC model predicts the (3,0) band should be undetectably faint.

There are several other potential features in Figure 8 at wavelengths greater than 1600\AA . Given the 1σ statistical error bars, several of these appear to be real. However, systematic errors introduced by our subtraction of the solar spectrum after modeling the atmospheric absorption and surface reflectance are likely much greater than the statistical uncertainty. We therefore urge caution in interpreting these features.

6. SPATIAL DISTRIBUTION OF AIRGLOW EMISSIONS

From the left-hand panel of Figure 1, the geometry of the Airglow3 observations is such that while the field of view of detector row 16 lies almost entirely on the disk of Pluto, rows 15 and 17 (zero-indexed) lie almost entirely off the limb, spanning a range of tangent altitudes from 0-1920 km (0–1.6 Pluto radii). No airglow emissions were detected in either of these rows. We suggest this is a consequence of gravitational diffusion and limb darkening. Methane (CH_4) is the dominant absorber below $\sim 1450\text{\AA}$. Because of its low molecular weight, it has a larger scale height than most other atmospheric species. As a result, there is considerably less of these heavier species between New Horizons and the $\tau = 1$ level in Pluto’s atmosphere along the tangential line of sight. For example, using the Young et al. (2018) atmospheric model, shown in Figure 4, the column density of N_2 above the $\tau = 1$ level at the LBH bands is $\sim 3.5\times$ lower for rows 15 and 17 than it is for row 16. This decrease in apparent column density renders the already faint emission lines below our detection threshold.

7. CONCLUSIONS AND FUTURE WORK

The main conclusions of our paper are as follows:

1. The brightness of IPM Lyman α at a heliocentric distance of 32.5 AU in the direction of Pluto ($\alpha=18^h2^m38.7^s$, $\delta = -14^\circ37'37''.2$), as seen from the New Horizons spacecraft is 133.4 ± 0.6 R. Lyman β has a brightness of 0.24 ± 0.02 R, and we place a 3σ upper limit of 0.10 R on the brightness of He I 584Å.
2. Although Pluto's atmosphere is completely opaque at Lyman α , it is optically thin ($\tau_v < 1$) for photons with $\lambda > 1425$ Å. These FUV photons can break molecular bonds and drive photolysis on the surface. We suggest this has important consequences for surface weathering and could explain why the areas on Pluto that receive the most insolation, averaged over its orbit, are darker and redder than the poles.
3. Pluto's surface reflectance between 1400-1850Å is approximately wavelength-independent with an I/F of 0.17. This is the first measurement of Pluto's reflectance in the FUV.
4. We detected a new species in Pluto's atmosphere in absorption: methylacetylene (C_3H_4 , or propyne). In our observations, methylacetylene has a column density of approximately 5×10^{15} cm $^{-2}$, corresponding to a column-integrated mixing ratio of 1.6×10^{-6} . This could provide an important constraint for photochemical models of Pluto's atmosphere.
5. We have detected airglow emissions from N_2 , NI, NII, HI, and CO in Pluto's upper atmosphere. Detected emissions range in brightness from a few tenths of a Rayleigh to 29.3 ± 1.9 R for Lyman α .
6. The discovery of the NII multiplet at 1085Å is the first direct detection of ions in Pluto's atmosphere. However, since this multiplet results from the prompt emission of NII after the dissociative photoionization of N_2 , it is not diagnostic of ionospheric density.

We suggest several areas ripe for future work. First, we examined only the most promising subset of the Alice airglow observations, selected for their relatively long integration time and proximity to Pluto. Second, more of the solar spectrum is absorbed by Pluto's atmosphere/surface between 1500–1580Å than we can account for in our modeling. Following our discovery of methylacetylene, we suggest that it is likely there are one or more additional minor species in Pluto's atmosphere that have not yet been identified. Third, in our modeling, we have neglected the physics of Pluto's haze particles, which are complex and likely to vary with altitude. A careful treatment of Pluto's atmospheric haze is required to improve upon our upper limit of Pluto's surface reflectance. Finally, although our atmospheric model produces a reasonable match to Pluto's observed airglow spectrum, there is significant room for improvement. A careful treatment of the radiative transfer effects of emissions and absorption by multiple hydrocarbon species along the line of sight could yield a significantly better match to the observations.

ACKNOWLEDGMENTS

Financial support for this work was provided by NASA’s New Horizons project via contracts NASW-02008 and NAS5- 97271/TaskOrder30. We thank the New Horizons Mission team for making these observations possible. Werner Curdt provided the high spectral-resolution solar models. We gratefully acknowledge the solar spectroscopic data available from the LASP Interactive Solar Irradiance Data Center (LISIRD) <http://lasp.colorado.edu/lisird/>. Atmospheric profiles of C_3H_4 were kindly provided by M. L. Wong and Y. Yung (2017, private communication) based on their photochemical model (Wong et al. 2017). We thank Paul Feldman for constructive discussion and providing model spectra of the CO Fourth Positive bands. We are grateful to the anonymous reviewer for their helpful comments and the editorial staff for their understanding and accommodation of the delay between receipt of the reviewer’s comments and submission of the revised manuscript.

Facility: New Horizons

APPENDIX

A. DATA REDUCTION

In this appendix, we discuss the data reduction techniques described in Section 3 in more detail. The first data reduction step is to correct for the dead time of the detector, for each of the individual exposures. This correction is necessary because the detector electronics take a finite amount of time to process each detected count, during which the detector is “dead”, i.e. it is insensitive to any additional counts. Thus, each detected count is weighted by a factor of $1/(1 - \tau C)$, where $\tau=18 \mu\text{s}$ is the time constant of the electronics and C is the average count rate during the exposure (Stern et al. 2008).

After the dead time correction we then use the “stim pixels” to correct the location of the spectrum in data space (Stern et al. 2008). Unlike many classes of detectors such as (CCDs), the Alice detector does not have any physical pixels. Instead, when an ultraviolet photon strikes the front surface of the MCP, it produces a photoelectron. As the front and back surfaces of the MCP are held at an electric potential of several thousand volts, the electron is accelerated into the pores of the microchannel plate, where it strikes the walls, liberating more electrons. The resulting cascade produces a cloud of ~ 6 million electrons (~ 1 pC of charge) exiting the back surface of the MCP, which then strikes the readout anode. The detector electronics compares the times when the charge pulse is detected on one side of the readout anode to when the signal is detected on the other side of the anode, after traveling through a delay circuit. The difference in timing determines how the event is mapped from physical space on the readout anode to data space. Changes in temperature affect the resistivity of the readout anode, which, in turn, affects the relative timing of the charge pulses. Thus,

an event that occurs at the same physical location can be mapped into a different location in data space, depending on temperature. To correct for this, the electronics produces artificial charge pulses at known physical locations on opposite sides of the detector, which allows for a linear correction to the apparent location of detected photons.

After applying the dead time correction factor and the stim pixel correction we co-add all the data and divide by the total exposure time of 3,900 s. We then subtract a dark countrate image from the data. The dark countrate image was produced by summing Alice images acquired with the airglow aperture door closed and dividing by the total integration time. In total, 10,720 seconds of dark integration time was obtained during Active Checkout 8 in July 2014 and 10,800 seconds of dark integration time was acquired during the post-encounter calibration campaign of July 2016. Typical dark count rates are of the order of $0.004 \text{ counts s}^{-1} \text{ px}^{-1}$ and show no evidence of temporal change.

REFERENCES

- Ajello, J. M., Stevens, M. H., Stewart, I., et al. 2007, *Geophys. Res. Lett.*, 34, L24204, doi: [10.1029/2007GL031555](https://doi.org/10.1029/2007GL031555)
- Bagenal, F., Horányi, M., McComas, D. J., et al. 2016, *Science*, 351, aad9045, doi: [10.1126/science.aad9045](https://doi.org/10.1126/science.aad9045)
- Bishop, J., & Feldman, P. D. 2003, *Journal of Geophysical Research (Space Physics)*, 108, 1243, doi: [10.1029/2001JA000330](https://doi.org/10.1029/2001JA000330)
- Bockelée-Morvan, D., Lellouch, E., Biver, N., et al. 2001, *A&A*, 377, 343, doi: [10.1051/0004-6361:20011040](https://doi.org/10.1051/0004-6361:20011040)
- Broadfoot, A. L., Atreya, S. K., Bertaux, J. L., et al. 1989, *Science*, 246, 1459, doi: [10.1126/science.246.4936.1459](https://doi.org/10.1126/science.246.4936.1459)
- Chamberlain, J. W., & Hunten, D. M. 1987, *Theory of planetary atmospheres. An introduction to their physics and chemistry.*
- Chen, F. Z., & Wu, C. Y. R. 2004, *JQSRT*, 85, 195, doi: [10.1016/S0022-4073\(03\)00225-5](https://doi.org/10.1016/S0022-4073(03)00225-5)
- Cheng, A. F., Summers, M. E., Gladstone, G. R., et al. 2017, *Icarus*, 290, 112, doi: [10.1016/j.icarus.2017.02.024](https://doi.org/10.1016/j.icarus.2017.02.024)
- Courtin, R., Gautier, D., & McKay, C. P. 1995, *Icarus*, 114, 144, doi: [10.1006/icar.1995.1050](https://doi.org/10.1006/icar.1995.1050)
- Curdt, W., Brekke, P., Feldman, U., et al. 2001, *A&A*, 375, 591, doi: [10.1051/0004-6361:20010364](https://doi.org/10.1051/0004-6361:20010364)
- Elliot, J. L., Dunham, E. W., Bosh, A. S., et al. 1989, *Icarus*, 77, 148, doi: [10.1016/0019-1035\(89\)90014-6](https://doi.org/10.1016/0019-1035(89)90014-6)
- Evans, J. S., Stevens, M. H., Lumpe, J. D., et al. 2015, *Geophys. Res. Lett.*, 42, 9040, doi: [10.1002/2015GL065489](https://doi.org/10.1002/2015GL065489)
- Gladstone, G. R., Allen, M., & Yung, Y. L. 1996, *Icarus*, 119, 1, doi: [10.1006/icar.1996.0001](https://doi.org/10.1006/icar.1996.0001)
- Gladstone, G. R., Pryor, W. R., & Stern, S. A. 2015, *Icarus*, 246, 279, doi: [10.1016/j.icarus.2014.04.016](https://doi.org/10.1016/j.icarus.2014.04.016)
- Gladstone, G. R., Retherford, K. D., Egan, A. F., et al. 2012, *Journal of Geophysical Research (Planets)*, 117, E00H04, doi: [10.1029/2011JE003913](https://doi.org/10.1029/2011JE003913)
- Gladstone, G. R., Stern, S. A., Ennico, K., et al. 2016, *Science*, 351, aad8866, doi: [10.1126/science.aad8866](https://doi.org/10.1126/science.aad8866)
- Greaves, J. S., Helling, C., & Friberg, P. 2011, *MNRAS*, 414, L36, doi: [10.1111/j.1745-3933.2011.01052.x](https://doi.org/10.1111/j.1745-3933.2011.01052.x)
- Hendrix, A. R., & Hansen, C. J. 2008, *Icarus*, 193, 323, doi: [10.1016/j.icarus.2007.06.030](https://doi.org/10.1016/j.icarus.2007.06.030)

- Hinson, D. P., Linscott, I. R., Young, L. A., et al. 2017, *Icarus*, 290, 96, doi: [10.1016/j.icarus.2017.02.031](https://doi.org/10.1016/j.icarus.2017.02.031)
- Hubbard, W. B., Hunten, D. M., Dieters, S. W., Hill, K. M., & Watson, R. D. 1988, *Nature*, 336, 452, doi: [10.1038/336452a0](https://doi.org/10.1038/336452a0)
- Jain, S. K., & Bhardwaj, A. 2015, *Icarus*, 246, 285, doi: [10.1016/j.icarus.2014.08.032](https://doi.org/10.1016/j.icarus.2014.08.032)
- Jain, S. K., Stewart, A. I. F., Schneider, N. M., et al. 2015, *Geophysical Research Letters*, 42, 9023, doi: [10.1002/2015GL065419](https://doi.org/10.1002/2015GL065419)
- Kameta, K., Kouchi, N., Ukai, M., & Hatano, Y. 2002, *Journal of Electron Spectroscopy and Related Phenomena*, 123, 225, doi: [https://doi.org/10.1016/S0368-2048\(02\)00022-1](https://doi.org/10.1016/S0368-2048(02)00022-1)
- Krasnopolsky, V. A. 2020, *Icarus*, 335, 113374, doi: [10.1016/j.icarus.2019.07.008](https://doi.org/10.1016/j.icarus.2019.07.008)
- Krasnopolsky, V. A., & Cruikshank, D. P. 1999, *J. Geophys. Res.*, 104, 21979, doi: [10.1029/1999JE001038](https://doi.org/10.1029/1999JE001038)
- Lellouch, E., de Bergh, C., Sicardy, B., Käuff, H. U., & Smette, A. 2011, *A&A*, 530, L4, doi: [10.1051/0004-6361/201116954](https://doi.org/10.1051/0004-6361/201116954)
- Lellouch, E., Gurwell, M., Butler, B., et al. 2017, *Icarus*, 286, 289, doi: [10.1016/j.icarus.2016.10.013](https://doi.org/10.1016/j.icarus.2016.10.013)
- Li, C., Zhang, X., Gao, P., & Yung, Y. 2015, *ApJL*, 803, L19, doi: [10.1088/2041-8205/803/2/L19](https://doi.org/10.1088/2041-8205/803/2/L19)
- Luspay-Kuti, A., Mandt, K., Jessup, K.-L., et al. 2017, *MNRAS*, 472, 104, doi: [10.1093/mnras/stx1362](https://doi.org/10.1093/mnras/stx1362)
- Mousis, O., Lunine, J. I., Mandt, K. E., et al. 2013, *Icarus*, 225, 856, doi: [10.1016/j.icarus.2013.03.008](https://doi.org/10.1016/j.icarus.2013.03.008)
- Niemann, H. B., Atreya, S. K., Demick, J. E., et al. 2010, *Journal of Geophysical Research (Planets)*, 115, E12006, doi: [10.1029/2010JE003659](https://doi.org/10.1029/2010JE003659)
- Olkin, C. B., Spencer, J. R., Grundy, W. M., et al. 2017, *AJ*, 154, 258, doi: [10.3847/1538-3881/aa965b](https://doi.org/10.3847/1538-3881/aa965b)
- Owen, T. C., Roush, T. L., Cruikshank, D. P., et al. 1993, *Science*, 261, 745, doi: [10.1126/science.261.5122.745](https://doi.org/10.1126/science.261.5122.745)
- Roble, R. G., & Hays, P. B. 1972, *Planet. Space Sci.*, 20, 1727, doi: [10.1016/0032-0633\(72\)90194-8](https://doi.org/10.1016/0032-0633(72)90194-8)
- Samson, J. A. R., Chung, Y., & Lee, E.-M. 1991, *JChPh*, 95, 717, doi: [10.1063/1.461424](https://doi.org/10.1063/1.461424)
- Schneider, N. M., Deighan, J. I., Jain, S. K., et al. 2015, *Science*, 350, 0313, doi: [10.1126/science.aad0313](https://doi.org/10.1126/science.aad0313)
- Siegmund, O. H., Tremsin, A. S., Vallerga, J. V., et al. 2000, in *Proc. SPIE*, Vol. 4140, X-Ray and Gamma-Ray Instrumentation for Astronomy XI, ed. K. A. Flanagan & O. H. Siegmund, 188–198
- Stern, S. A. 2008, *SSRv*, 140, 3, doi: [10.1007/s11214-007-9295-y](https://doi.org/10.1007/s11214-007-9295-y)
- Stern, S. A., Slater, D. C., Scherrer, J., et al. 2007, *SSRv*, 128, 507, doi: [10.1007/s11214-006-9035-8](https://doi.org/10.1007/s11214-006-9035-8)
- . 2008, *Space Sci. Rev.*, 140, 155, doi: [10.1007/s11214-008-9407-3](https://doi.org/10.1007/s11214-008-9407-3)
- Stern, S. A., Feaga, L. M., Schindhelm, E., et al. 2015, *Icarus*, 256, 117, doi: [10.1016/j.icarus.2015.04.023](https://doi.org/10.1016/j.icarus.2015.04.023)
- Stevens, M. H. 2001, *J. Geophys. Res.*, 106, 3685, doi: [10.1029/1999JA000329](https://doi.org/10.1029/1999JA000329)
- Stevens, M. H., Evans, J. S., & Gladstone, G. R. 2013, in *The Pluto System on the Eve of Exploration by New Horizons: Perspectives and Predictions*, Laurel, MD, 165
- Stevens, M. H., Evans, J. S., Lumpe, J., et al. 2015, *Icarus*, 247, 301, doi: [10.1016/j.icarus.2014.10.008](https://doi.org/10.1016/j.icarus.2014.10.008)
- Stevens, M. H., Meier, R. R., Conway, R. R., & Strobel, D. F. 1994, *J. Geophys. Res.*, 99, 417, doi: [10.1029/93JA01996](https://doi.org/10.1029/93JA01996)
- Stevens, M. H., Gustin, J., Ajello, J. M., et al. 2011, *Journal of Geophysical Research (Space Physics)*, 116, A05304, doi: [10.1029/2010JA016284](https://doi.org/10.1029/2010JA016284)
- Stevens, M. H., Siskind, D. E., Evans, J. S., et al. 2017, *Geophysical Research Letters*, 44, 4709, doi: [10.1002/2017GL072717](https://doi.org/10.1002/2017GL072717)

- Strickland, D. J., Bishop, J., Evans, J. S., et al. 1999, *JQSRT*, 62, 689, doi: [10.1016/S0022-4073\(98\)00098-3](https://doi.org/10.1016/S0022-4073(98)00098-3)
- Strobel, D. F., & Zhu, X. 2017, *Icarus*, 291, 55, doi: [10.1016/j.icarus.2017.03.013](https://doi.org/10.1016/j.icarus.2017.03.013)
- Summers, M. E., Strobel, D. F., & Gladstone, G. R. 1997, *Chemical Models of Pluto's Atmosphere*, ed. S. A. Stern & D. J. Tholen, 391
- Throop, H. B., Stern, S. A., Parker, J. W., Gladstone, G. R., & Weaver, H. A. 2009, in *AAS/Division for Planetary Sciences Meeting Abstracts*, Vol. 41, AAS/Division for Planetary Sciences Meeting Abstracts #41, 68.20
- Tyler, G. L., Linscott, I. R., Bird, M. K., et al. 2008, *SSRv*, 140, 217, doi: [10.1007/s11214-007-9302-3](https://doi.org/10.1007/s11214-007-9302-3)
- Wagner, J. K., Hapke, B. W., & Wells, E. N. 1987, *Icarus*, 69, 14, doi: [10.1016/0019-1035\(87\)90003-0](https://doi.org/10.1016/0019-1035(87)90003-0)
- Wong, M. L., Fan, S., Gao, P., et al. 2017, *Icarus*, 287, 110, doi: [10.1016/j.icarus.2016.09.028](https://doi.org/10.1016/j.icarus.2016.09.028)
- Woods, T. N., Eparvier, F. G., Bailey, S. M., et al. 2005, *Journal of Geophysical Research (Space Physics)*, 110, A01312, doi: [10.1029/2004JA010765](https://doi.org/10.1029/2004JA010765)
- Young, L. A., Cook, J. C., Yelle, R. V., & Young, E. F. 2001, *Icarus*, 153, 148, doi: [10.1006/icar.2001.6662](https://doi.org/10.1006/icar.2001.6662)
- Young, L. A., Elliot, J. L., Tokunaga, A., de Bergh, C., & Owen, T. 1997, *Icarus*, 127, 258, doi: [10.1006/icar.1997.5709](https://doi.org/10.1006/icar.1997.5709)
- Young, L. A., Stern, S. A., Weaver, H. A., et al. 2008, *SSRv*, 140, 93, doi: [10.1007/s11214-008-9462-9](https://doi.org/10.1007/s11214-008-9462-9)
- Young, L. A., Kammer, J. A., Steffl, A. J., et al. 2018, *Icarus*, 300, 174, doi: <https://doi.org/10.1016/j.icarus.2017.09.006>
- Zhang, X., Strobel, D. F., & Imanaka, H. 2017, *Nature*, 551, 352, doi: [10.1038/nature24465](https://doi.org/10.1038/nature24465)